On Embedded Element Radiation Function and Beam Direction of Wide-Scanning Array Antennas

N.B. When citing this work, cite the original published paper.

(article starts on next page)

On Embedded Element Radiation Function and Beam Direction of Wide-Scanning Array Antennas

PRABHAT KHANAL[ID] (Graduate Student Member, IEEE), AND JIAN YANG[ID] (Senior Member, IEEE)

Electrical Engineering Department, Chalmers University of Technology, 41296 Gothenburg, Sweden

CORRESPONDING AUTHOR: P. KHANAL (e-mail: prabhat@chalmers.se)

ABSTRACT This paper presents a rigorous new analytical derivation of the theorem on the embedded element radiation function of ideally infinite planar array antennas, along with a formula for accurately calculating the main beam direction of finite-sized array antennas based on the theorem. It validates the previously established formula of the embedded element radiation function, where the amplitude is proportional to $\sqrt{\cos\theta}$, based on the intuitive reasoning that the effective area of an element should be proportional to its projected area in the direction of interest angle θ, provided that the array antenna has no grating lobes for the full scan, no surface waves, no losses, and active impedance matched. More importantly, the new analytical derivation can accurately predict the embedded element radiation function in cases where there are grating lobes for the array antenna with the full scan, which the intuitive area projection reasoning cannot provide. The theorem concludes that the array's active element reflection coefficient and inter-element spacing fully determine the embedded element radiation function in all cases. Utilizing this theorem, a new formula for the element phase progression is derived to accurately steer the main beam in the desired direction of the array with a finite number of elements. Several verification cases of wide-scanning array antennas are presented, and the comparisons between numerical simulations, measurements, theoretical results, and some interesting conclusions are discussed in the paper.

INDEX TERMS Antenna arrays, array factor, beam steering, embedded element function, wide-scanning.

I. INTRODUCTION

ARRAY antennas are among the most important types of antennas [1], consistently prioritized in design whenever steerable beams, specific beam shapes, low side-lobe levels, or other fully controllable antenna functions are required [2], [3], [4]. Researchers find the investigation and analysis of array antenna properties and characteristics particularly compelling. Research topics in array antenna technologies include beam steering [2], [5], sidelobe suppression with different element excitation schemes [4], [6], mutual couplings between elements [7], [8], [9], scan blindness avoidance [10], [11], edge effects on radiation patterns and reflection coefficient [12], [13], [14].

One intriguing topic in array antenna properties is the embedded element radiation function. The far-field function of an array antenna results from the product of the embedded element radiation function and the array factor. The embedded element radiation pattern refers to the radiation pattern of an antenna element within an array when the other elements are terminated by matched loads. In this paper, we distinguish between the radiation function for individual antenna elements and the far-field function for the entire array antenna. An intriguing question for antenna engineers is whether a general function exists for the embedded element radiation function in large array antennas, regardless of the types of elements used.

Hannan proposed in 1964 [15] that the element gain should vary as $\cos\theta$, based on the intuitive reasoning that an element's effective area should be proportional to its projected area in the direction of interest. However, this reasoning may be considered somewhat weak.

Based on our rigorous derivation, we find that the embedded element pattern of an array over the scanning range without grating lobes indeed follows $\sqrt{cos\theta}$ (antenna gain

$cos\theta$). Therefore, explaining this phenomenon as resulting from the projection of the element area onto the plane normal to the far-field vector seems valid. However, this intuitive reasoning does not accurately predict the embedded element pattern over the scanning range with grating lobes. Schuss observed in [16] that the theoretical embedded element radiation function, based on cosine projection of the far-field vector, does not match an array's measured embedded element pattern over the scan range with a grating lobe.

In this paper, we employ the Fourier transform on the array factor to rigorously derive the embedded element radiation function. This approach not only confirms Hannan's intuitive reasoning over the scanning range without grating lobes but also extends it to the scanning range with a grating lobe. Thus, our approach surpasses Hannan's intuitive reasoning and Schuss's cosine projection theory, offering novel insights into array performance.

Another phenomenon observed in the array antennas is that the beam direction of the array differs slightly from what is predicted by the array factor with a designed element phase progression. For example, in [17], [18], [19], [20], it can be observed that the measured radiation patterns have the main beams at the directions with slightly smaller angles than the claimed ones. We also encountered this phenomenon when using the element phase progression of $\Delta\Phi_x = -k_x d \sin\theta_0$ to steer the main beam directions in our array antennas. This observation prompted our investigation in this study.

The classical derivation of the array factor [21] assumes an array antenna with an infinitely large number of elements. Its main beam is pointed to the direction $(\theta_0, 0)$ (without losing generality, we set $\phi_0 = 0$ for the main beam direction here) using a progressive phase shift along the $x-$axis of $\Delta\Phi_x = -kd_x \sin\theta_0$. Along the $y-$axis of $\Delta\Phi_y = 0$, where k is the wave number, and d_x is the element spacing along the $x-$axis. However, in an array of a finite number of elements, this progressive phase shift causes the main beam to point in a slightly different direction than $(\theta_0, 0)$. Therefore, using the embedded element radiation function derived in this work, we have formulated a method to calculate the correct phase progression for the main beam to precisely point in the desired direction of a finite-sized array antenna.

To verify the theorem and formula presented in the paper, several designed array antennas in the literature have been taken as examples. It is concluded that the performance of the examples in the literature aligns perfectly with that of our analysis.

II. THEOREM ON EMBEDDED ELEMENT RADIATION FUNCTION

THEOREM ON EMBEDDED ELEMENT RADIATION FUNCTION OF AN IDEAL WIDE-SCANNING PHASED ARRAY ANTENNA WITHOUT GRATING LOBES:

In an ideal large planar phased array antenna (asymptotically an infinitely large phased array), the amplitude of the normalized embedded element radiation function is $|G_0(\theta, \phi)| = \sqrt{\cos\theta}$ in a ϕ plane, regardless of the type of elements used in the array antenna, as long as the array antenna has no grating lobes, no surface waves, no ohmic loss, and maintains perfect impedance matching with zero active reflection coefficient at all elements' ports when the main beam is steered over a range of $\theta \in [0, \theta_{\max}]$ in the ϕ plane.

Proof: The derivation of this proof follows the derivation of the power integral in [21], as shown in the Appendix section of this paper. ∎

If the array antenna is designed such that there are no grating lobes when the main beam direction θ_0 of the array antenna is steered over $[0, \theta_{\max}]$ in the $\phi = \phi_0$ plane, then from (31) in the Appendix:

$$P = |G(\theta_0, \phi_0)|^2 \frac{(2\pi)^2}{k^2 \cos\theta_0 (d_x d_y)^2} P_{pq}. \tag{1}$$

For the case when the main beam direction is at the broadside direction, i.e., $\theta_0 = 0$, we have

$$P(\theta_0 = 0) = |G(0, \phi_0)|^2 \frac{(2\pi)^2}{k^2 (d_x d_y)^2} P_{pq}. \tag{2}$$

Here, we further assume that the antenna uses lossless materials (no ohmic loss in the antenna), a perfect active impedance match (i.e., the active reflection coefficient is 0), and no surface waves to cause radiation in directions other than those defined by the array factor. The power integral should be the same for both cases of the main beam at $\theta = 0$ and at $\theta = \theta_0$. Therefore, from (1) and (2) we get

$$|G(0, \phi_0)|^2 \frac{(2\pi)^2 P_{pq}}{k^2 (d_x d_y)^2} = |G(\theta_0, \phi_0)|^2 \frac{(2\pi)^2 P_{pq}}{k^2 \cos\theta_0 (d_x d_y)^2},$$

which leads to

$$\frac{|G(\theta_0, \phi_0)|^2}{|G(0, \phi_0)|^2} = \cos\theta_0,$$

where we can also write $G(0, \phi_0) = G(0, 0)$. Hence, the amplitude of the normalized embedded element radiation function $|G_0(\theta_0, \phi_0)|$ in $\phi = \phi_0$ plane is

$$|G_0(\theta_0, \phi_0)| = \frac{|G(\theta_0, \phi_0)|}{|G(0, 0)|} = \sqrt{\cos\theta_0}, \tag{3}$$

A. THEOREM EXTENSION I

The condition of perfect active impedance match for all element ports in the above theorem is unnecessary. Assume that for the nth, element the active reflection coefficient is $\Gamma_n(\theta_0, \phi_0)$ when the main beam is scanned to (θ_0, ϕ_0). Thus, the input power to the nth element is

$$P_{in,n}(\theta_0, \phi_0) = \alpha_n^2 \left(1 - |\Gamma_n(\theta_0, \phi_0)|^2\right) \tag{4}$$

where α_n is the weighting coefficient of the nth element excitation for the aperture distribution. Therefore, the total input power to the array antenna is

$$P_{in,tot}(\theta_0, \phi_0) = \sum_{n=1}^{N} \alpha_n^2 \left(1 - |\Gamma_n(\theta_0, \phi_0)|^2\right) \tag{5}$$

Then, from (1) and (2), the ratio of power integral $P(\theta_0, \phi_0)$ when the main beam is at (θ_0, ϕ_0) to power integral $P(0, 0)$ when the main beam is at boresight $(0, 0)$, can be written as

$$\frac{P(\theta_0, \phi_0)}{P(0, 0)} = \frac{\sum_{n=1}^{N} \alpha_n^2 \left(1 - |\Gamma_n(\theta_0, \phi_0)|^2\right)}{\sum_{n=1}^{N} \alpha_n^2 \left(1 - |\Gamma_n(0, 0)|^2\right)}, \quad (6)$$

which leads to

$$|G_0(\theta_0, \phi_0)| = \frac{|G(\theta_0, \phi_0)|}{|G(0, 0)|}$$

$$= \sqrt{\cos \theta_0} \sqrt{\frac{\sum_{n=1}^{N} \alpha_n^2 \left(1 - |\Gamma_n(\theta_0, \phi_0)|^2\right)}{\sum_{n=1}^{N} \alpha_n^2 \left(1 - |\Gamma_n(0, 0)|^2\right)}}. \quad (7)$$

If we further assume a uniform aperture distribution and a very large array (ignoring the edge effects), where $\alpha_n = \alpha$ and $\Gamma_n(\theta_0, \phi_0) = \Gamma(\theta_0, \phi_0)$ for all elements, we have

$$|G_0(\theta_0, \phi_0)| = \sqrt{\cos \theta_0} \sqrt{\frac{1 - |\Gamma(\theta_0, \phi_0)|^2}{1 - |\Gamma(0, 0)|^2}}. \quad (8)$$

In simulations, obtaining $\Gamma(\theta, \phi)$ using a unit cell with periodic boundaries is simple and fast. In measurements, having a measured embedded element radiation function is straightforward. This allows a fast calculation for the embedded element radiation function and, consequently, the whole far-field function of the array from the simulated $\Gamma(\theta, \phi)$ using (8) during simulations, as well as a quick estimation of the active reflection coefficient for each element from the measured embedded element patterns using (8) during measurements. Therefore, we avoid the challenging simulations for the embedded element radiation function and the complex measurements for the active reflection coefficient for each element.

B. THEOREM EXTENSION II
Now, we assume that there is one grating lobe at θ_g when the main beam θ_0 is scanned over $[\theta_{\max}, 90°]$ in a ϕ_0 plane. Then, from (31) in the Appendix, we have

$$P = \left(\frac{|G(\theta_0, \phi_0)|^2}{\cos \theta_0} + \frac{|G(\theta_g, \phi_0)|^2}{\cos \theta_g}\right) \frac{(2\pi)^2}{k^2 (d_x d_y)^2} P_{pq}. \quad (9)$$

With the same assumption as in Extension I, we have

$$\frac{|G_0(\theta_0, \phi_0)|^2}{\cos \theta_0} + \frac{|G_0(\theta_g, \phi_0)|^2}{\cos \theta_g} = \frac{1 - |\Gamma(\theta_0, \phi_0)|^2}{1 - |\Gamma(0, 0)|^2}. \quad (10)$$

where,

$$\theta_g = \arcsin\left(\sin \theta_0 \pm \frac{\lambda}{d}\right)$$

Therefore, (10) is an equation involving the function $|G_0(\theta_0, \phi_0)|$.

Assuming the embedded element radiation function within $\theta_0 \in [\theta_{\max}, 90°]$ follows the same format as within $\theta_0 \in [0°, \theta_{\max}]$ with a different coefficient α

$$|G_0(\theta_0, \phi_0)| = \alpha \sqrt{\cos(\theta_0)} \sqrt{\frac{1 - |\Gamma(\theta_0, \phi_0)|^2}{1 - |\Gamma(0, 0)|^2}},$$
$$\text{when } \theta_0 \in [\theta_{\max}, 90°]. \quad (11)$$

From (10) and (11), we have

$$\alpha = \sqrt{\frac{1}{1 + \beta}}, \quad (12)$$

where

$$\beta = \frac{1 - |\Gamma(\theta_g, \phi_0)|^2}{1 - |\Gamma(\theta_0, \phi_0)|^2}.$$

Note that $\theta_g = f(\theta_0)$; hence, β is a function of θ_0. If $|\Gamma(\theta_0, \phi_0)| = 0$ and $|\Gamma(\theta_g, \phi_0)| = 0$, then $\beta = 1$ and $\alpha = 1/\sqrt{2}$.

From (8) and (11), we conclude that at the boundary $\theta_{\max}$ between the non-grating-lobe region and one-grating-lobe region, the embedded element radiation function is not continuous. There is a $\alpha \approx 1/\sqrt{2}$ difference, which is reasonable given the sudden appearance of a grating lobe and the split of radiated power between the grating lobe and the main lobe.

The theorem with these two extensions is referred to as the Embedded Element theorem, where Hannan's intuitive reasoning cannot obtain extension II.

C. DISCUSSION I
From the proof above, it initially appeared that the normalized embedded element radiation function is independent of ϕ. However, this assertion is not entirely accurate. The scanning range $\theta \in [0, \theta_{\max}]$, without grating lobes, varies across different ϕ planes; thus, $\theta_{\max}$ is a function of ϕ in general. When a phased array antenna is designed to avoid grating lobes and surface waves, achieving perfect active impedance match across the full scanned main beam direction θ over $\in [0, 90°]$ in all ϕ planes results in the amplitude of the normalized embedded element radiation function always being $\sqrt{\cos \theta_0}$, regardless of the type of antenna elements used or their spacings (including different spacings in the x- and y-axes, provided they are smaller than half wavelength).

D. DISCUSSION II
The directivity of a planar phased array antenna can be expressed by [21]

$$D = \frac{4\pi \left|\mathbf{G}(\theta_0, \phi_0) AF(k \sin \theta_0 \cos \phi_0, k \sin \theta_0 \sin \phi_0) \cdot \hat{\mathbf{co}}^*\right|^2}{P}. \quad (13)$$

As shown in Fig. 1, the amplitudes of all grating lobes in the array factor $|AF(k \sin \theta_0 \cos \phi_0, k \sin \theta_0 \sin \phi_0)|$
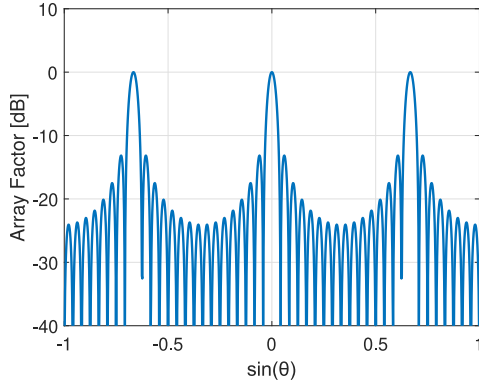
FIGURE 1. The array factor of a 16×16 element array with element spacing $d = 1.5\lambda$ shows that all the grating lobes have the same amplitude and beamwidth in $\sin\theta$ scale.

FIGURE 2. Projection of the aperture into the scan direction.

are identical, irrespective of θ_0 and ϕ_0. Therefore, when the main beam is steered to $\theta_0 \in [0, \theta_{\max}]$, the term $|AF(k\sin\theta_0\cos\phi_0, k\sin\theta_0\sin\phi_0)|$ remains constant. Therefore, the normalized directivity D_0 can be written as

$$D_0(\theta_0, \phi_0) = \frac{D(\theta_0, \phi_0)}{D(0, 0)} = \cos\theta_0.$$

Thus, the factor of $\cos\theta_0$ is introduced in the directivity calculation for planar array antennas as

$$D = e_{\mathrm{grt}}e_{\mathrm{pol}}e_{\mathrm{ill}}\cos\theta_0 D_{\max}, \tag{14}$$

where e_{grt}, e_{pol} and e_{ill} are the grating efficiency, the polarization efficiency, and the illumination efficiency, respectively. Detailed expressions are found in [21]. Here, we emphasize the following point. It is a widespread explanation that the factor of $\cos\theta_0$ is introduced due to the projection of the array aperture into the scan direction, as shown in Fig. 2. However, we have demonstrated a new perspective on the introduction of the $\cos\theta_0$ factor to the embedded element radiation function. An important and unambiguous concept is now established: when there are no grating lobes (e_{grt}=1) and all other sub-efficiencies (e_{pol} and e_{ill}) remain constant, the directivity decreases solely by $\cos\theta_0$ as the main beam direction θ_0 is scanned over $[0, \theta_{\max}]$. It is incorrect to calculate the directivity drop as

$$\frac{|G(\theta_0, \phi_0)|^2}{|G(0, 0)|^2} \cdot \cos\theta_0,$$

since this formula applies $\cos\theta_0$ twice.

E. DISCUSSION III
An isolated element pattern is the radiation pattern of a single antenna element radiating in free space, meaning there is only one element present without any array environment. In contrast, the embedded element pattern is the radiation pattern of an element within an array when only that specific element is excited, with all other elements terminated with matched loads. In Fig. 3, E_m represents the isolated element pattern, while $E_{m,embedded}$ represents the embedded element pattern of the mth element.
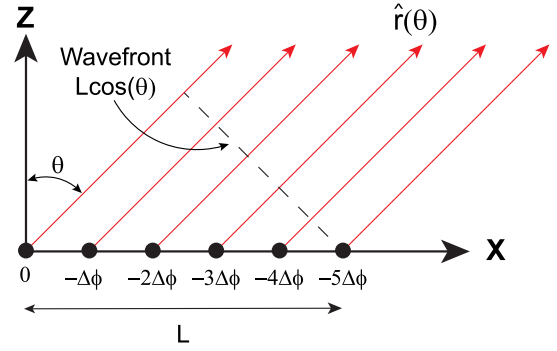
Due to mutual coupling, elements that are terminated with matched loads also get excited by the power equivalent to the mutually coupled power. Half of this power is absorbed by the matched load, and the other half is re-radiated (according to the maximum power transfer theorem), as illustrated in Fig. 4. Consequently, the embedded element radiation function is a combination of the radiation from the excited element and the re-radiation from all other mutually coupled elements terminated with matched loads in the array. Therefore, the embedded element radiation function already includes mutual coupling in it.

III. FORMULA FOR ACCURATE BEAM DIRECTION
FORMULA FOR ACCURATE BEAM DIRECTION WITH LARGE SCANNING ANGLES FOR FINITE-SIZED ARRAY ANTENNAS:
In an ideal large planar array antenna (approaching an infinitely large planar array) without grating lobes, progressive phase shifts of $\Delta\Phi_x = kd_x\sin\theta_0$ between antenna elements along the x-axis and $\Delta\Phi_y = 0$ along the y-axis are applied to steer its main beam toward the direction $(\theta_0, 0)$, where k is the wave number $k = 2\pi/\lambda$ and d_x the element spacing along the x-axis. It is assumed here, without loss of generality and for simplicity, that the main beam is steered with θ_0 in the $\phi = 0$ plane.

However, in a practical finite-sized phased array antenna, the main beam actually points to a direction θ_{mb} which is slightly smaller than θ_0 with the progressive phase shift $\Delta\Phi_x$. The relationship between the actual beam direction θ_{mb} and the desired beam direction θ_0 with the progressive phase shift $\Delta\Phi_x = kd_x\sin\theta_0$ is defined by the following equation:

$$\sin\theta_{\mathrm{mb}} + \frac{n}{2}\cos^2\theta_{\mathrm{mb}}(\sin\theta_{\mathrm{mb}} - \sin\theta_0) = 0, \tag{15}$$

where

$$n = \frac{-3}{20\log(\cos(\sin(\frac{\theta_{3\mathrm{dB}}}{2})))},$$

and $\theta_{3\mathrm{dB}}$ is the half 3dB beamwidth of the array antenna when the main beam is in boresight $\theta_0 = 0$.
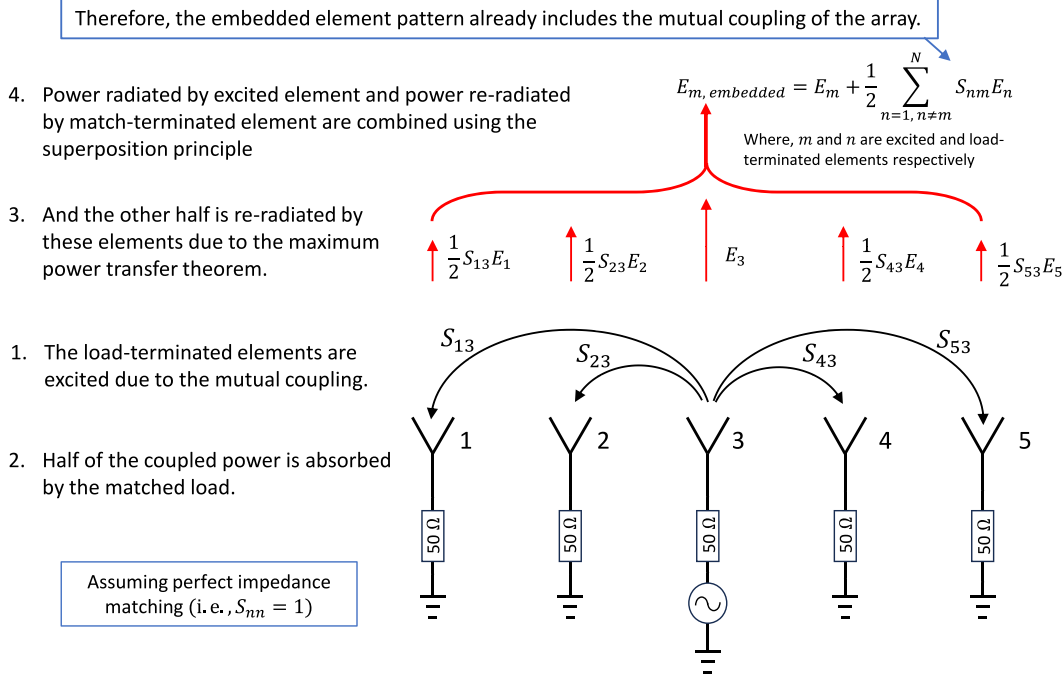
FIGURE 3. The explanation of how the embedded element pattern already includes the mutual coupling of the array antenna.
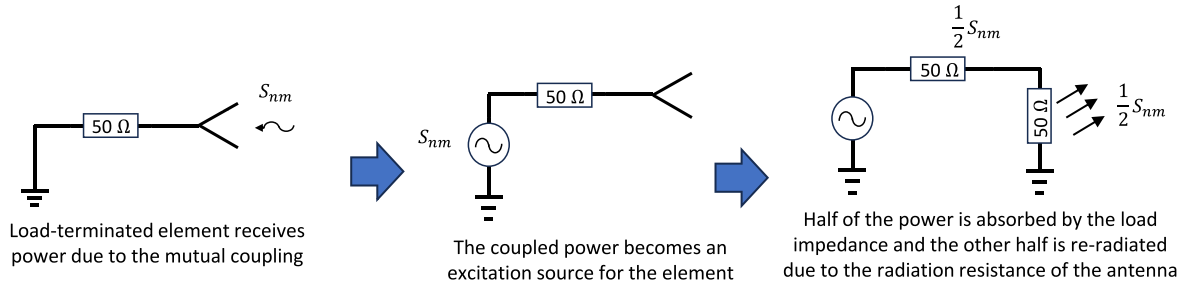

FIGURE 4. The explanation of how a load-terminated element re-radiates due to the maximum power transfer theorem.

To steer the main beam to θ_0, the correct progressive phase shift $\Delta\Phi_{xcorr}$ should be

$$\Delta\Phi_{xcorr} = \Delta\Phi_x + \Delta\Phi_{xextra}$$
$$= kd_x \sin\theta_0 \left(1 + \frac{2}{n\cos^2\theta_0}\right) \quad (16)$$

Derivation Since the beam shape of an array factor remains the same in the scaling of $\sin\theta$, as shown in Fig. 5, the main beam of an array factor can be approximated regardless of its direction by

$$AF_{approx}(\theta, \phi) \approx \cos^n\left(\frac{\sin\theta - \sin\theta_0}{2}\right), \quad (17)$$

where θ_0 denotes the direction of the main beam of the array factor, and n is determined by the half 3dB beamwidth θ_{3dB} of the array antenna when the main beam is at boresight $\theta_0 = 0$ as [21]

$$n = \frac{-3}{20\log\left(\cos\left(\sin\left(\frac{\theta_{3dB}}{2}\right)\right)\right)}, \quad (18)$$

where

$$\theta_{3dB} = \arcsin\left(\frac{0.445\lambda}{L_{eff}}\right)$$

$$L_{eff} = \sqrt{(d_x N_x \cos\phi)^2 + (d_y N_y \sin\phi)^2}.$$

For an $N_x \times N_y$ array with element spacing d_x and d_y in the $x-$ and $y-$ directions, respectively, (17) and (18) accurately represent the main beam of the array factor up to the 3dB beamwidth at any $\phi-$plane. Assuming no grating lobes, $\phi = 0$ and $L_{eff} = L_{xeff} = d_x N_x$, the far-field function $G_a(\theta, 0)$ becomes
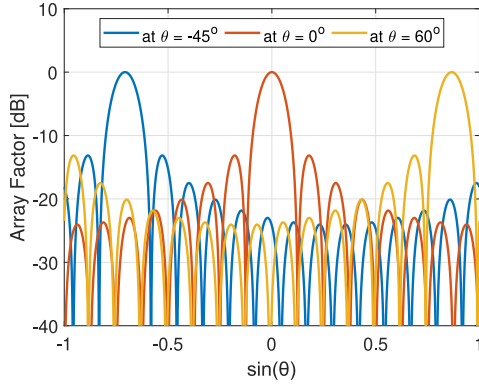
$$G_a(\theta, 0) = G(\theta, 0)AF_{approx}(\theta, 0)$$

FIGURE 5. Array factor of 16×16 element array with element spacing $d = 0.5\lambda$ when steered in different directions in the scaling of $\sin\theta$ for x-axis.

$$= \sqrt{\cos\theta}\cos^n\left(\frac{\sin\theta - \sin\theta_0}{2}\right).$$

The embedded element radiation function $G(\theta, 0)$ tapers the array factor $AF(\theta, 0)$ (see Figs. 6–8). Therefore, the maximum beam direction of the array far-field function $G_a(\theta, 0)$ does not align with the maximum beam direction of the array factor $AF(\theta, 0)$. The derivative of $G_a(\theta, 0)$ over θ is

$$\frac{\mathrm{d}G_a(\theta, 0)}{\mathrm{d}\theta} = \frac{\mathrm{d}\left[G(\theta, 0)AF_{\text{approx}}(\theta, 0)\right]}{\mathrm{d}\theta}$$
$$= -\frac{1}{2\sqrt{\cos\theta}}\cos^n\left(\frac{\sin\theta - \sin\theta_0}{2}\right)$$
$$\left(\sin\theta + n\cos^2\theta\,\frac{\sin\left(\frac{\sin\theta - \sin\theta_0}{2}\right)}{\cos\left(\frac{\sin\theta - \sin\theta_0}{2}\right)}\right).$$

The actual main beam direction θ_{mb} is found where the derivative equals zero

$$\sin\theta_{\text{mb}} + n\cos^2\theta_{\text{mb}}\,\frac{\sin\left(\frac{\sin\theta_{\text{mb}} - \sin\theta_0}{2}\right)}{\cos\left(\frac{\sin\theta_{\text{mb}} - \sin\theta_0}{2}\right)} = 0 \qquad (19)$$

Given that θ_{mb} slightly differs from θ_0, it follows that $|\sin\theta_{\text{mb}} - \sin\theta_0| << 1$. Thus,

$$\sin\left(\frac{\sin\theta_{\text{mb}} - \sin\theta_0}{2}\right) \approx \frac{\sin\theta_{\text{mb}} - \sin\theta_0}{2},$$
$$\cos\left(\frac{\sin\theta_{\text{mb}} - \sin\theta_0}{2}\right) \approx 1.$$

Hence, (19) becomes

$$\sin\theta_{\text{mb}} + \frac{n}{2}\cos^2\theta_{\text{mb}}(\sin\theta_{\text{mb}} - \sin\theta_0) = 0. \qquad (20)$$

Since $\sin\theta_{\text{mb}}$, n and $\cos^2\theta_{\text{mb}}$ are positive values, (20) will hold true only when $(\sin\theta_{\text{mb}} - \sin\theta_0) < 0$, which means that $\theta_{\text{mb}} < \theta_0$. Therefore, in order for the main beam of $G_a(\theta, 0)$ to point to the direction θ_0, an additional progressive phase shift $\Delta\Phi_{x\text{extra}}$ is required to steer the main beam of the array factor $AF_{\text{approx}}(\theta, 0)$ to the direction $(\theta_0 + \Delta\theta, 0)$, where
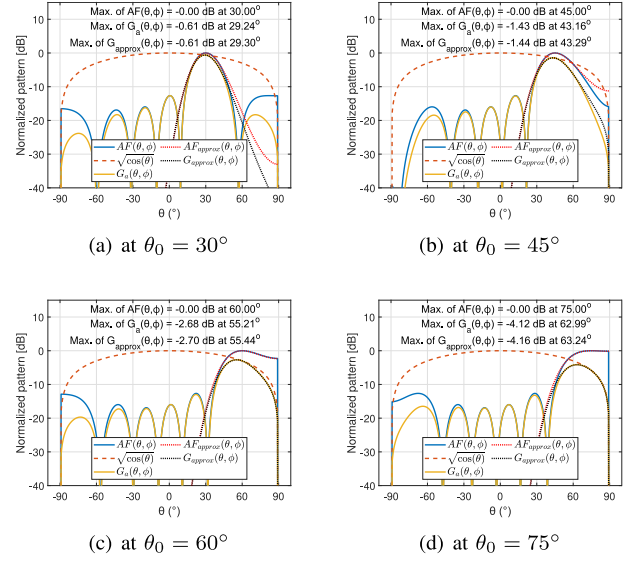

(a) at $\theta_0 = 30°$ (b) at $\theta_0 = 45°$

(c) at $\theta_0 = 60°$ (d) at $\theta_0 = 75°$

FIGURE 6. Patterns of the 7×7 element array of ideal $\sqrt{\cos\theta}$ antenna elements with element spacing $d = 0.42\lambda$, and progressive phase shifts $\Delta\Phi$ at different beam scanning angles.
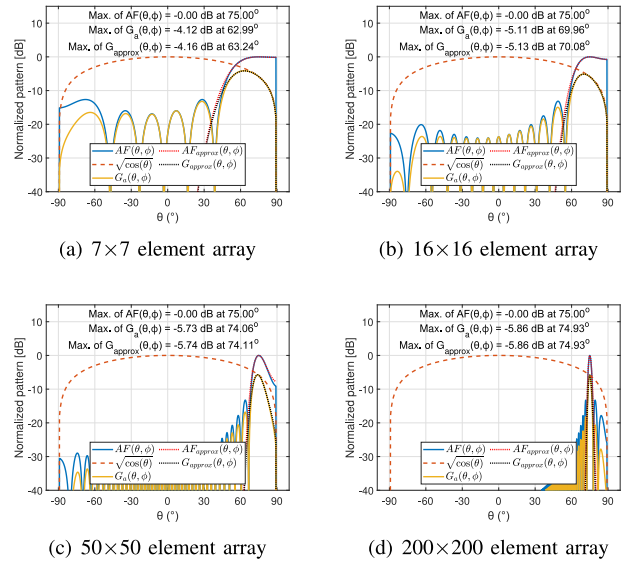

(a) 7×7 element array   (b) 16×16 element array

(c) 50×50 element array   (d) 200×200 element array

FIGURE 7. Patterns of the 7×7, 16×16, 50×50, and 200×200 element arrays of ideal $\sqrt{\cos\theta}$ antenna elements with element spacing $d = 0.42\lambda$, and progressive phase shifts $\Delta\Phi$ at $\theta_0 = 75°$.

$\Delta\theta$ will be solved by the following procedure. The correct progressive phase shift of $\Delta\Phi_{x\text{corr}}$ is required as

$$\Delta\Phi_{x\text{corr}} = \Delta\Phi_x + \Delta\Phi_{x\text{extra}} = kd_x\sin(\theta_0 + \Delta\theta)$$
$$= kd_x\sin\theta_0\cos\Delta\theta + kd_x\cos\theta_0\sin\Delta\theta$$
$$\approx kd_x\sin\theta_0 + kd_x\cos\theta_0\sin\Delta\theta \qquad (21)$$

Since $\cos\Delta\theta \approx 1$ due to $\Delta\theta \approx 0$, we have we have $\Delta\Phi_{x\text{extra}} = kd_x\cos\theta_0\sin\Delta\theta$.

And, the identity in (20) becomes

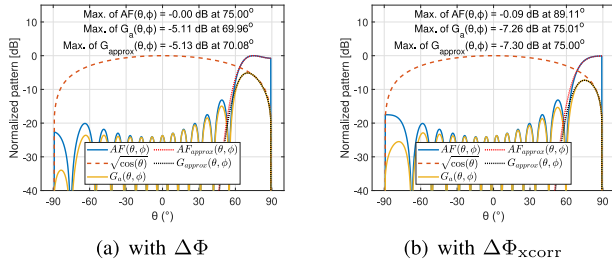$$\sin\theta_0 + \frac{n}{2}\cos^2\theta_0(\sin\theta_0 - \sin(\theta_0 + \Delta\theta)) = 0,$$

(a) with $\Delta\Phi$ (b) with $\Delta\Phi_{xcorr}$

FIGURE 8. Patterns of the 16×16 element array of ideal $\sqrt{\cos\theta}$ antenna elements with element spacing $d = 0.42\lambda$, and progressive phase shifts $\Delta\Phi$ and $\Delta\Phi_{xcorr}$, which are calculated using the main beam direction $\theta_0 = 75°$.

$$\sin\theta_0 - \frac{n}{2}\cos^2\theta_0\cos\theta_0\sin\Delta\theta = 0,$$

$$\cos\theta_0\sin\Delta\theta = \sin\theta_0\frac{2}{n\cos^2\theta_0}. \quad (22)$$

From (21) and (22), it leads to

$$\Delta\Phi_{xextra} = kd_x\cos\theta_0\sin\Delta\theta = kd_x\sin\theta_0\frac{2}{n\cos^2\theta_0}. \quad (23)$$

Therefore, the correct progressive phase shift $\Delta\Phi_{xcorr}$ in order to point the main beam of a finite-sized phased array to direction $(\theta_0, 0)$ is

$$\begin{aligned}\Delta\Phi_{xcorr} &= \Delta\Phi_x + \Delta\Phi_{xextra} \\ &= kd_x\sin\theta_0 + kd_x\sin\theta_0\frac{2}{n\cos^2\theta_0} \\ &= kd_x\sin\theta_0\left(1 + \frac{2}{n\cos^2\theta_0}\right). \quad (24)\end{aligned}$$

A. DISCUSSION I
In the following discussions, the inter-element spacing d_x is always selected such that there are no grating lobes within the visible region $\theta \in [-90°, 90°]$ in $\phi = 0$ plane, for example,

$$d_x \le \frac{\lambda}{2 + \lambda/L_{\text{eff}}}.$$

As shown in Figs. 6 and 7, the progressive phase shift $\Delta\Phi_x$ maximizes the amplitude of the array factor $AF(\theta, 0)$ at direction $(\theta_0, 0)$. However, due to the tapering effect of the embedded element pattern $G(\theta, 0) = \sqrt{\cos\theta}$, the actual maximum of the array antenna $G_a(\theta, \phi)$ occurs at θ_{mb} which is smaller than θ_0. The beam-pointing error $\Delta\theta = \theta_0 - \theta_{mb}$ becomes significant at large beam scan angles due to the sharper tapering of the embedded element pattern (see Fig. 6). Similarly, the array factor beamwidth of a not-large-sized array antenna is broad, creating a large beam-pointing error $\Delta\theta$. This error becomes smaller as the array size increases, as shown in Fig. 7.

The correct progressive phase shift $\Delta\Phi_{xcorr}$ is used to point the main beam of the antenna array in the direction $(\theta_0, 0)$ as shown in Fig 8. It steers the main beam of the array factor $AF(\theta, 0)$ beyond θ_0 so that the maximum of the array antenna $G_a(\theta, 0)$ occurs in direction $(\theta_0, 0)$. In a very
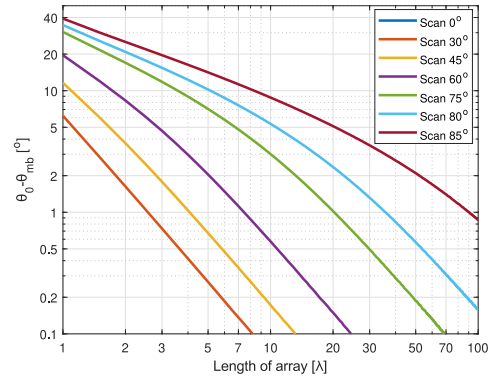

FIGURE 9. The beam-pointing error $\Delta\theta = \theta_0 - \theta_{mb}$ when scanning at different directions at different sizes of the array antenna.

large-sized array, the beam-pointing error $\Delta\theta$ will be very small, and the extra progressive phase shift $\Delta\Phi_{xextra} \approx 0$ since n becomes very large.

B. DISCUSSION II
The corrected progressive phase shift $\Delta\Phi_{xcorr}$ points the main beam of the finite array at the desired angle by making the main beam of the array factor scan beyond the desired angle, so that the main beam of the whole array is at the desired angle due the tapering from the embedded element radiation function. However, from the impedance point of view, the array excitation is the same as scanning in the direction where the array factor is pointing, which is wider than the desired angle. Therefore, the larger beam-pointing error $\Delta\theta = \theta_0 - \theta_{mb}$ degrades the active reflection coefficient of a finite array. Instead of correcting a large beam-pointing error using $\Delta\theta_{corr}$, we should use a larger array size, which results in a small beam-pointing error, and then apply the correction using $\Delta\theta_{corr}$. This approach minimizes the degradation of the active reflection coefficient is minimal. Fig. 9 shows the beam-pointing error at different scanning angles for different array sizes. This figure can be used to choose the appropriate array size for an acceptable beam-pointing error and its corresponding active reflection coefficient degradation. It can also be used to quickly identify how large the array antenna needs to be to scan up to a certain angle.

C. DISCUSSION III
The main beam direction θ_{mb} of the array, when using the progressive phase shift $\Delta\Phi_x$ in (20), and the correct progressive phase shift $\Delta\Phi_{xcorr}$ required to steer the beam at the desired direction $(\theta_0, 0)$ in (24), are derived for uniformly excited arrays. For non-uniformly excited arrays or arrays with a different shape than rectangular aperture, the results may vary, but the same derivation procedure can be applied.

IV. VERIFICATION WITH REAL ANTENNA ARRAYS
To verify the theorem and the formulas presented above, we have selected three antenna arrays of different antenna elements and sizes from the literature:
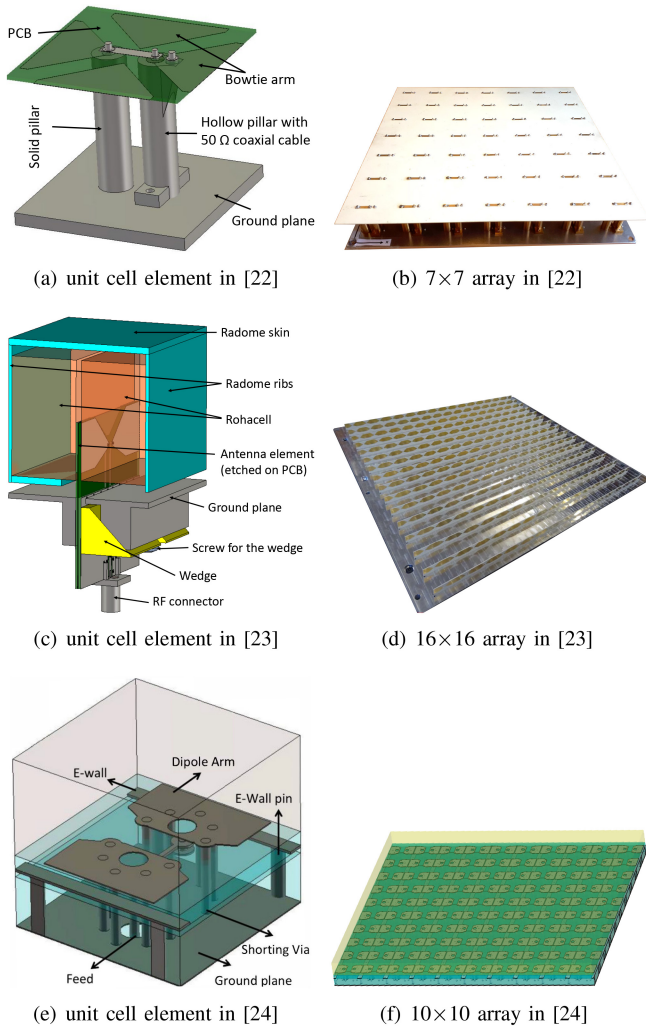
(a) unit cell element in [22]

(b) 7×7 array in [22]

(c) unit cell element in [23]

(d) 16×16 array in [23]

(e) unit cell element in [24]

(f) 10×10 array in [24]

FIGURE 10. Pictures of the antenna elements and their arrays in [22], [23], [24].

(a) E-plane, central element

(b) H-plane, central element

(c) E-plane, averaged

(d) H-plane, averaged

FIGURE 11. E- and H-plane embedded element patterns of the central element and the averaged patterns of all 49 elements in the 7×7 element array [22] at 3 GHz.

- The 7×7 array of cross-bowties [22]
- The 16×16 array of vertical-bowties [23]
- The 10×10 array of tightly-coupled-dipoles [24]

The dimensions and descriptions of these arrays and their antenna elements are provided in their corresponding articles.

A. VERIFICATION OF THE EMBEDDED ELEMENT RADIATION FUNCTION THEOREM

Figs. 10a and 10b show pictures of the cross-bowtie unit cell element and its 7×7 element array antenna prototype presented in [22]. The elements are horizontally polarized bowtie antennas with the element spacing of 0.4λ at 3GHz in both E- and H-planes, ensuring no grating lobes in any ϕ-planes for $\theta \in [-90°, 90°]$. The antenna can scan the main beam over $\theta \in [-60°, 60°]$ in the E-plane (azimuth plane) and $\theta \in [-15°, 15°]$ in the H-plane (elevation plane) with a low active reflection coefficient.

Fig. 11 shows the E- and H-plane embedded element patterns of the central element and the averaged E- and H-plane embedded element patterns of all 49 elements in
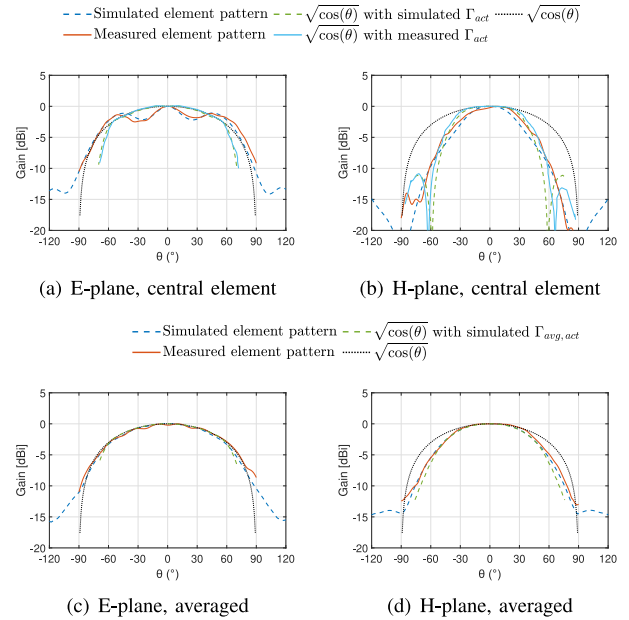
the array. The simulated and measured embedded element patterns agree well with the theoretical embedded element pattern $\sqrt{\cos\theta}$ in (3) over $\theta \in [-60°, 60°]$ in the E-plane and $\theta \in [-15°, 15°]$ in the H-plane. The ripples in the simulated and measured patterns of the central element are primarily due to the array size being relatively small (only 7×7 elements). These ripples are significantly reduced in the averaged element patterns. For θ out of $[-15°, 15°]$ in the H-plane, high active reflection coefficients (see in [22]) cause the embedded element pattern to drop faster than $\sqrt{\cos\theta}$.

Fig. 11 also shows the theoretical embedded radiation patterns ($\sqrt{\cos\theta}$ with Γ_{act} and $\Gamma_{\mathrm{avg, act}}$), calculated using (8). Γ_{act} and $\Gamma_{\mathrm{avg, act}}$ are the active reflection coefficients of the central element and the average active reflection of the whole array, respectively. The measurement result of the average active reflection coefficient of the whole array is not available, so no measured data is included. When scanning at wide angles, the main beam of the antenna array decreases, and eventually, a sidelobe becomes higher than the main beam, limiting the scanning range. Therefore, the theoretical embedded radiation pattern is calculated only up to the angle where the main beam remains higher than all sidelobes instead of over the full $[-90°, 90°]$ range.

There is a good match between the simulated/measured embedded element patterns and the theoretical ones in (8) in Fig. 11. In the E-plane, the measured and simulated embedded central element patterns match the theoretical ones quite well within $\theta \in [-60°, 60°]$ due to the low Γ_{act}. Beyond $\pm 60°$, the embedded central element pattern decreases sharply due to high Γ_{act}. In the H-plane, the measured and simulated embedded element patterns also match the theoretical ones, validating (8).

(a) E-plane, central element

(b) H-plane, central element
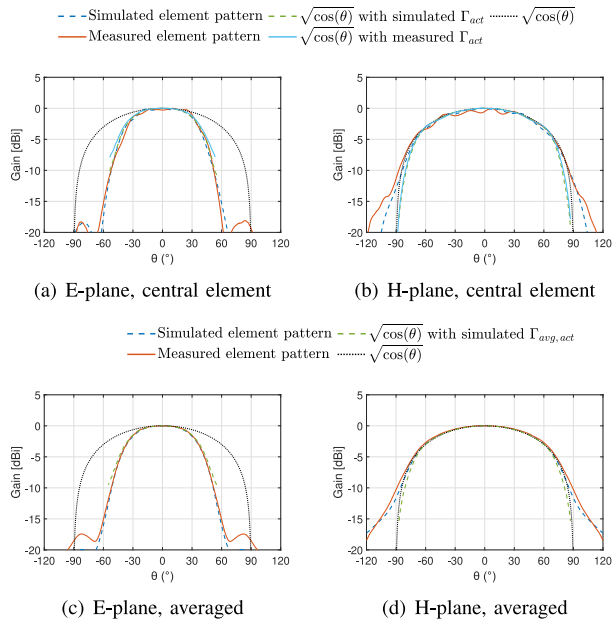
(c) E-plane, averaged

(d) H-plane, averaged

FIGURE 12. E- and H-plane embedded element patterns of the central element and the averaged patterns of all 256 elements in the 16×16 element array [23] at 2.7 GHz.

(a) E-plane, central element

(b) H-plane, central element

(c) E-plane, averaged

(d) H-plane, averaged

FIGURE 13. Simulated E- and H-plane embedded element patterns of the central element and the averaged simulated patterns of all 100 elements in the 10×10 element array [24] at 25 GHz.

Figs. 10c and 10d show pictures of the vertical-bowtie unit cell and its 16×16 element array antenna prototype presented in [23]. The elements are vertically polarized bowtie antennas integrated with a curved radome, with element spacing of 0.38λ at 2.7 GHz in both E- and H-planes, ensuring no grating lobes in any ϕ-plane over $\theta \in [-90°, 90°]$. The array can scan the main beam over $\theta \in [-75°, 75°]$ in the H-plane (azimuth plane) and $\theta \in [-15°, 15°]$ in the E-plane (elevation plane) with a low active reflection coefficient.

Fig. 12 shows the E- and H-plane embedded element patterns of the central element and the averaged E- and H-plane embedded element patterns of all 256 elements in the array. There is a good agreement between the theoretical patterns calculated by (3), the simulated patterns, and the measured embedded element radiation patterns for $\theta \in [-75°, 75°]$ in the H-plane and $\theta \in [-15°, 15°]$ in the E-planes can be observed. The ripples in the simulated and measured patterns of the central element are much smaller now due to the larger array size (16×16 elements).

Fig. 12 also shows a good agreement between the central and averaged embedded element patterns and the theoretical ones calculated by (8). The measurement result of the average active reflection coefficient of the whole array is not available, so it is not included. The agreement is better than that of the 7×7 cross-bowtie array because the 16×16 vertical-bowtie array is larger, reducing the influence from the array's edge on the central element. The ripples are further averaged out by averaging the embedded element patterns and active reflection coefficients of all the elements in the array. In the E-plane, the embedded element patterns predicated by (8) are more accurate than those predicted by (3), further validating (8).
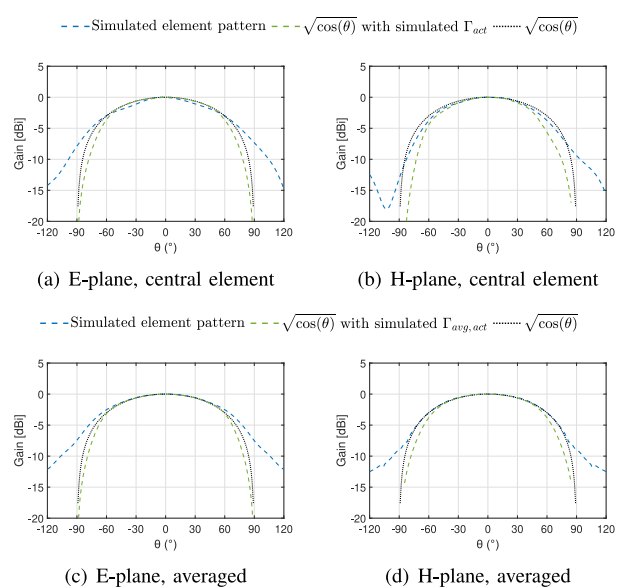
Figs. 10e and 10f show pictures of the tightly-coupled-dipole unit cell element and its 10×10 element array antenna model presented in [24] with element spacing of 0.25λ at 25 GHz in both E- and H-planes, ensuring no grating lobes in any ϕ-plane over $\theta \in [-90°, 90°]$. The antenna can scan the main beam over $\theta \in [-60°, 60°]$ in both E- and H-planes with a low active reflection coefficient.

Fig. 13 shows a good agreement between the simulated embedded element radiation patterns and the theoretical ones calculated using (8). Due to the high integration of the antenna array in [24], no measured embedded element radiation patterns or active reflection coefficients are available. For θ larger than 60° the edge effect is significant so the theoretical embedded element radiation patterns differ from the simulated ones.

For comparison, the simulated E- and H-plane radiation patterns of the cross-bowtie element [22], the vertical-bowtie element [23], and the tightly-coupled-dipole [24] element in the isolated environments (i.e., only one antenna element in free space) are shown in Fig. 14. These E- and H-plane radiation patterns of the isolated antenna elements in [22], [23], [24] are very different from each other and from $\sqrt{\cos\theta}$. However, the above verification shows that when the elements are in the array, the embedded element radiation patterns in both E- and H-planes become $\sqrt{\cos\theta}$ for $\theta_0 \in [0, \theta_{max}]$, when there are no grating lobes and good impedance matching.

We now investigate the scenario where there is one grating lobe in the far-field while steering the main beam of an array over $\theta \in [0, 90°]$, which occurs when the element spacing is between 0.5λ and λ. To explore this, we modified the 16×16 array antenna from [23] by increasing the element spacing to 65 mm (0.585λ at 2.7 GHz) and 80 mm (0.765λ
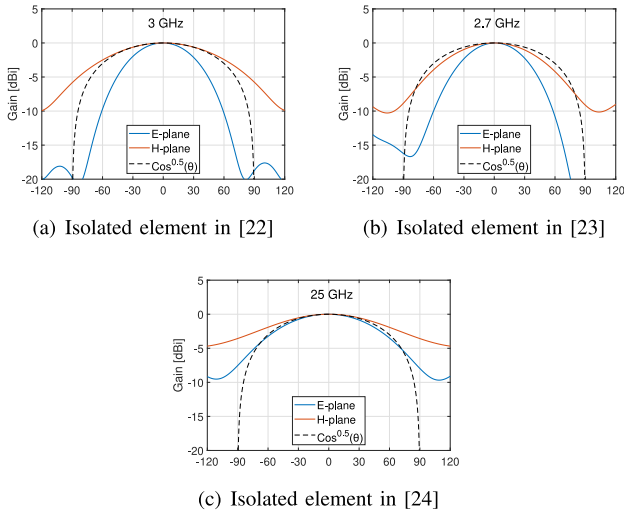
(a) Isolated element in [22]

(b) Isolated element in [23]

(c) Isolated element in [24]

FIGURE 14. Simulated E- and H-plane patterns of the isolated element antennas used in the arrays [22], [23] and [24] at 3 GHz, 2.7 GHz, and 25 GHz respectively.
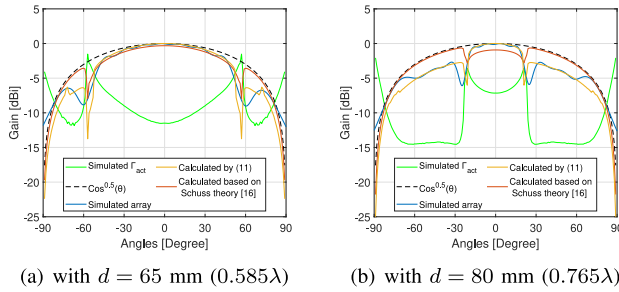

(a) with $d = 65$ mm (0.585λ)

(b) with $d = 80$ mm (0.765λ)

FIGURE 15. Simulated E-plane embedded element patterns of the 16×16 array [23] with inter-element spacing d of 65 mm (0.585λ) and 80 mm (0.765λ) at 2.7 GHz.

at 2.7 GHz), ensuring that we observe one grating lobe in the far-field at scan angle beyond $\theta_{\max} = 58°$ and $23°$, respectively. Then, we use the simulated results of these arrays to verify the theoretical one calculated by (11).

The embedded element radiation functions are calculated using (11) with simulated active reflection coefficients Γ_{act} for the two cases. Fig. 15 demonstrates that the simulated embedded element patterns and the calculated patterns using (11) exhibit good agreement, thereby verifying the theoretical formula in (11). Beyond $\theta_{\max}$, the embedded element radiation function decreases by approximately $\alpha \approx 1/\sqrt{2}$. Γ_{act} at each beam angle was simulated using a unit cell element in an infinite array environment to save simulation time; hence, it does not account for the finite-sized array effect present in the 16×16 array. Consequently, θ_{max} (the angles where the nulls occur between regions of no-grating lobe and one-grating lobe) slightly differ between the calculated embedded element radiation function and the simulated embedded element radiation pattern.

For comparison, Fig. 15 also includes the embedded element pattern calculated using the conventional formula presented by Schuss in [16], which is expressed as

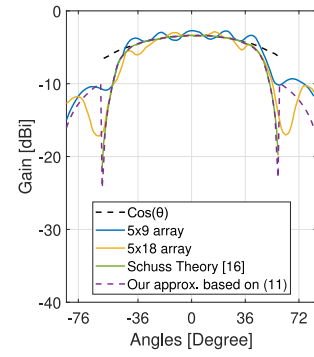$$|G_0(\theta_0, \phi_0)| = \sqrt{\cos\theta_0}\sqrt{1 - |\Gamma(\theta_0, \phi_0)|^2} \qquad (25)$$

FIGURE 16. Reproduction of a figure from Schuss in [16] depicting the measured and predicted E-plane embedded element patterns of the 5×9 and 5×18 arrays of rectangular patches at $f = 1.105f_0$, where one grating lobe is present in the array when scanning at $\theta > 60°$, together with our approximated embedded element pattern based on (11). The figure is reproduced with the original scaling.

This formula, based on the projection of the array area in the direction of θ, can be found in various literature sources including prominent antenna books such as [1] and [25]. Note that this formula closely resembles our formula (8). However, the main distinction is that our embedded element radiation function (8) is valid only up to the scan angle θ where grating lobes do not appear in the far-field pattern of the array. Once one grating lobe appears, (8) becomes invalid, and the embedded element radiation function transitions to that defined by (11). In contrast, the conventional embedded element radiation function (25) does not have such limitations. Therefore, up to the scan angle where no grating lobes are present, the calculated embedded element pattern using the conventional formula matches the simulated pattern. However, beyond this angle, when the grating lobes appear, the pattern calculated by Schuss theory [16] (the conventional calculation) no longer aligns with the simulated pattern.

Fig. 16 is a reproduction of a figure from [16] that shows the embedded element patterns of 5×9 and 5×18 microstrip arrays of rectangular patches at $f = 1.05f_0$, where one grating lobe appear in the far-field of the arrays when scanning beyond $60°$. The curve labeled "Schuss theory" in the figure represents the embedded element pattern predicted by Schuss in [16] based on the projection of the array area at θ direction concept (given by (25)). This curve matches well with the measured embedded element patterns for the 5×9 and 5×18 arrays up to the region where no grating lobes are present during scanning. However, the "Schuss theory" curve is not shown beyond $\pm 60°$ where one grating lobe appears in the array's far-field pattern. In contrast, using our (11), which is based on the conservation of energy theory, we can accurately predict the embedded element radiation even when one grating lobe appears, as shown by the curve "Our approx. based on (11)" in Fig. 16. Schuss in [16] did not provide the active reflection coefficient Γ_{act} data at each θ scan angle at $f = 1.05f_0$. Therefore, for the grating-lobe-free region ($\theta < 60°$), we obtain Γ_{act} using (25), and for the one-grating-lobe region, we estimated Γ_{act} under the assumption

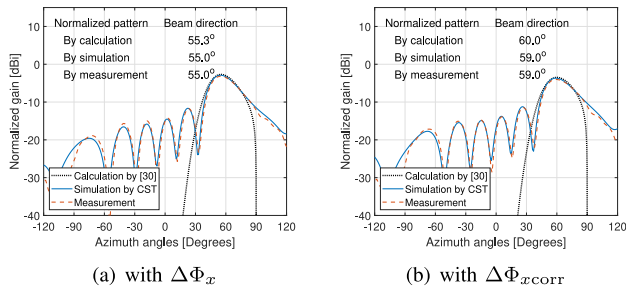(a) with $\Delta\Phi_x$ (b) with $\Delta\Phi_{x\mathrm{corr}}$

FIGURE 17. E-plane far-field radiation function of the 7×7 array in [22] at 3 GHz, using the progressive phase shift of $\Delta\Phi_x = 124.71°$, $\Delta\Phi_y = 0$ and $\Delta\Phi_{x\mathrm{corr}} = 133.90°$, $\Delta\Phi_y = 0$ when scanning at $\theta_0 = 60°$ in the E-plane.

(a) with $\Delta\Phi_x$ (b) with $\Delta\Phi_{x\mathrm{corr}}$

FIGURE 18. H-plane far-field radiation function of the 16×16 array in [23] at 2.7 GHz, using the progressive phase shift of $\Delta\Phi_x = 131.44°$, $\Delta\Phi_y = 0$ and $\Delta\Phi_{x\mathrm{corr}} = 139.15°$, $\Delta\Phi_y = 0$ when scanning at $\theta_0 = 75°$ in the H-plane.

that Γ_{act} is close to 1 only at two angles: $\theta = 60°$, where the grating lobe become visible in the far-field of the array at $\theta_g = -90°$, and when the main beam of the array is at $\theta = 90°$. For other angles, $\Gamma_{act} \le -10$ dB. Then, we used (11) to calculate our approximate embedded element pattern of the element in the Schuss's antenna array from [16], as shown in Fig. 16. It can be observed that our approximated embedded element pattern matches his measured embedded element pattern very well for the 5×18 array. However, for the 5×9 array, due to its size, there is a noticeable difference between the measured data and our calculated data.

Examples in Figs. 15 and 16 demonstrate that our embedded element pattern formula (11) for the case when one grating lobe is present in the array, is accurate and novel since this behavior has not been predicted by the conventional embedded element function theory.

B. VERIFICATION OF THE ACCURATE BEAM DIRECTION FORMULA

Figs. 17, 18 and 19 illustrate the E- & H-plane patterns of the far-field radiation functions of the 7×7 cross-bowtie element array, the 16×16 vertical-bowtie element array and the 10×10 tightly-coupled-dipole element array, respectively. These arrays are excited with uniform amplitude and a progressive phase shift of $\Delta\Phi$ and $\Delta\Phi_{\mathrm{corr}}$. Depending on the plane (E- or H-plane), $\Delta\Phi$ and $\Delta\Phi_{\mathrm{corr}}$ correspond to $\Delta\Phi_x$ and $\Delta\Phi_{x\mathrm{corr}}$ or $\Delta\Phi_y$ and $\Delta\Phi_{y\mathrm{corr}}$.

As shown, when the progressive phase shift is $\Delta\Phi$, the main beam of the array is directed at a smaller θ angle than the desired beam direction θ_0. Conversely, when the progressive phase shift is $\Delta\Phi_{x\mathrm{corr}}$, the main beam aligns closely with the desired direction θ_0. The H-plane far-field pattern of the 7×7 cross-bowtie array and the E-plane far-field pattern of the 16×16 vertical bowtie array are omitted from this comparison because they scan within a narrower range, ±15°, resulting in minimal beam-pointing errors.

Notice that, even with $\Delta\Phi_{\mathrm{corr}}$, the beam is still not exactly at θ_0 but slightly above and below θ_0 in the 7×7 cross-bowtie element array and the 10×10 tightly-coupled-dipole element array, respectively. This discrepancy arises because their array sizes are not sufficiently large, and their embedded element patterns do not follow precisely $G(\theta, \phi) = \sqrt{\cos\theta}$.
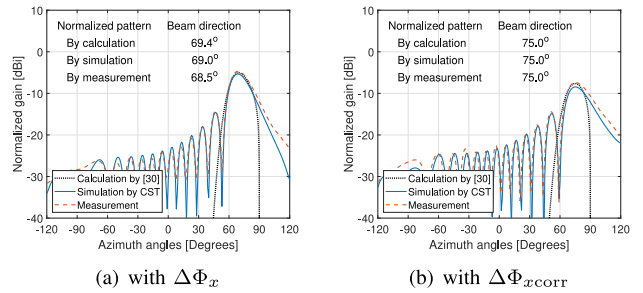

(a) with $\Delta\Phi_x$, E-plane   (b) with $\Delta\Phi_{x\mathrm{corr}}$, E-plane

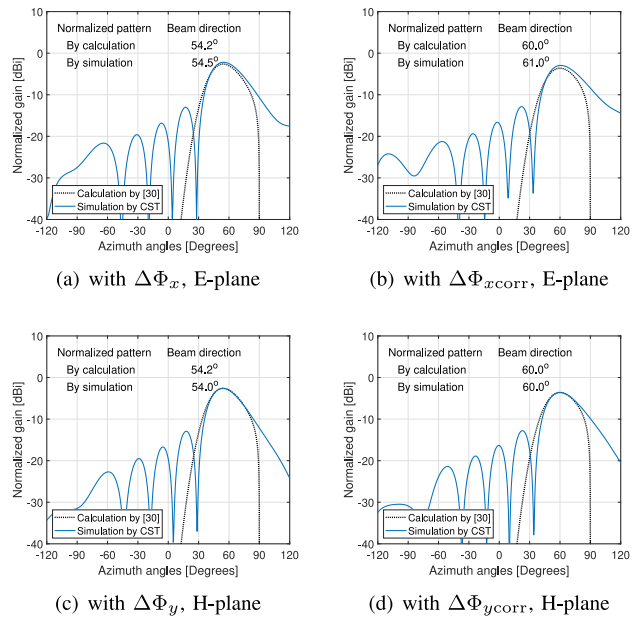(c) with $\Delta\Phi_y$, H-plane   (d) with $\Delta\Phi_{y\mathrm{corr}}$, H-plane

FIGURE 19. E- and H-plane far-field radiation functions of the 10×10 array in [22] at 25 GHz, using the progressive phase shifts of $\Delta\Phi_x = 79.94°$, $\Delta\Phi_y = 0$ and $\Delta\Phi_{x\mathrm{corr}} = 85.16°$, $\Delta\Phi_y = 0$ for the E-plane and $\Delta\Phi_y = 79.94°$, $\Delta\Phi_x = 0$ and $\Delta\Phi_{y\mathrm{corr}} = 85.16°$, $\Delta\Phi_x = 0$ for the H-plane when scanning at $\theta_0 = 60°$.

As shown in [26], the embedded element patterns of the central element deviate from $\sqrt{\cos\theta}$ for arrays of different sizes, resulting in a small beam-pointing error even with $\Delta\Phi_{\mathrm{corr}}$. However, $\Delta\Phi_{\mathrm{corr}}$ has significantly improved the alignment of the main beam closer to the desired direction θ_0 compared to $\Delta\Phi$, even for moderately sized arrays. For the larger 16×16 array, $\Delta\Phi_{\mathrm{corr}}$ precisely aligns the main beam with the desired direction θ_0.

In the derivation of the accurate beam direction formula in Section III, we assume that the embedded element radiation function $G(\theta, \phi) = \sqrt{\cos\theta}$ holds true for large-sized arrays, as derived and verified in Section II and the Section IV-A, respectively. However, for small-sized arrays, the embedded element radiation function may deviate from $G(\theta, \phi) = \sqrt{\cos\theta}$ due to different mutual coupling environments among elements and pronounced reflections from the edges of the array, which are more significant in smaller arrays. Consequently, there is no universal embedded

element radiation function for small-sized array antennas, and each array configuration requires individual analysis.

V. CONCLUSION

In this paper, we have presented an analytical derivation of the theorem regarding the embedded element radiation function of an infinite array. We have concluded that, under ideal conditions- where the array is designed without grating lobes, surface wave, and with perfect active impedance matching and low loss- the embedded element radiation function maintains an amplitude of $\sqrt{\cos\theta}$ regardless of the specific array elements used.

Additionally, we have extended this theorem to cover scenarios where the element's active reflection coefficient is non-ideal, and/or where one grating lobe appears in the far-field of the array when scanning over $\theta \in [0°, 90°]$. In such cases, the embedded element radiation function becomes a function of $\sqrt{\cos\theta}$, active impedance mismatch, and inter-element spacing (which determines the direction of the grating lobe).

Using this theorem, we derived a formula for accurately calculating beam direction and progressive phase shifts between elements in phased arrays with a finite number of antenna elements. We validated our theoretical findings by comparing them with simulations and measurements from several real-world array antenna designs found in the literature, demonstrating agreement between theory and simulations/measurements.

APPENDIX

The far-field function $G_a(\theta, \phi)$ of a large array antenna, as shown in Fig. 20 can be expressed as

$$G_a(\theta, \phi) = G(\theta, \phi)AF(\theta, \phi) \quad (26)$$

where $G(\theta, \phi)$ is the embedded radiation function of the elements in the array and $AF(\theta, \phi)$ is the array factor. For simplicity, we assume that the embedded radiation functions of all the elements in the array are the same, which occurs when the array is infinitely large with equal spacing along axes and uses identical antenna elements.

The power integral P, which relates to the radiated power P_{rad} from the antenna as

$$P = 2\eta P_{rad}$$

can be calculated using [21]

$$P = \int_0^{2\pi} \int_0^{\pi/2} |G_a(\theta, \phi)|^2 \sin\theta d\theta \quad (27)$$

where $\eta \approx 377 \, \Omega$ is the free space impedance. In (27), we assume $G_a(\theta, \phi) = 0$ when $\theta > \pi/2$ (i.e., no radiation field behind the array antenna aperture). This assumption holds for many antenna arrays backed by a ground plane or when the array elements are unidirectional. In realistic arrays, there may be some small backward radiation behind the aperture, which we ignore in this derivation.
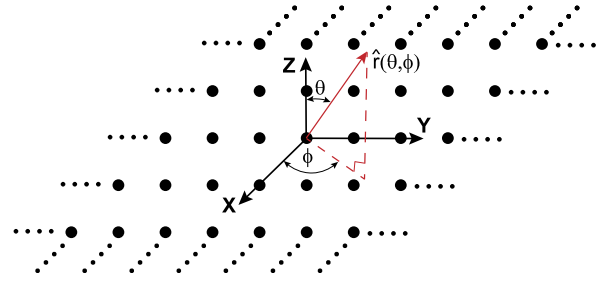

FIGURE 20. Illustration of an infinitely large array antenna, where dots represent the elements in the array.

The array factor $AF(\theta, \phi)$ can be expressed as an infinite grating-lobe sum as [21]

$$AF(\theta, \phi) = e^{j\phi_c} \frac{1}{d_x d_y} \sum_{p=-\infty}^{\infty} \sum_{q=-\infty}^{\infty} \tilde{A}\left(k_x - k_{\phi_x} - p\frac{2\pi}{d_x}, \right.$$
$$\left. k_y - k_{\phi_y} - q\frac{2\pi}{d_y}\right)$$
$$= AF(k_x, k_y) \quad (28)$$

where $\tilde{A}$ is the two-dimensional Fourier transform of the excitation distribution $A(x, y)$ over the aperture as

$$\tilde{A}(k_x, k_y) = \int_{-\infty}^{\infty} \int_{-\infty}^{\infty} A(x, y)e^{jk_x x}e^{jk_y y}dxdy \quad (29)$$

with the definition of excitation being zero outside the aperture A, and

$$k_x = \sin\theta \cos\phi \, k, \quad k_y = \sin\theta \sin\phi \, k.$$

We do the variable substitution as

$$k_\rho = k\sin\theta, \quad dk_\rho = k\cos\theta d\theta.$$

Then, the power integral P becomes

$$P = \int_0^{2\pi} \int_0^{\pi/2} |G(\theta, \phi)|^2 |AF(k_\rho \cos\phi, k_\rho \sin\phi)|^2$$
$$\frac{k_\rho}{k^2 \cos\theta} dk_\rho d\phi. \quad (30)$$

For a very large array in both x- and y-directions, the array factor produces much narrower beams (main beam and grating beams) compared to the embedded element radiation beam. Asymptotically, the array factor can be approximated as a sum of delta functions. In the k_ρ space, all grating lobes have the same amplitude and beamwidth, regardless of their location. Therefore, (30) can be written as

$$P = \sum_{pq} |G(\theta_{pq}, \phi_{pq})|^2 \frac{(2\pi)^2}{k^2 \cos\theta_{pq}(d_x d_y)^2} P_{pq}, \quad (31)$$

where the sum is taken over all pq grating lobes in the visible region, and

$$P_{pq} = \frac{1}{(2\pi)^2} \int_0^{2\pi} \int_0^k |\tilde{A}(k_x - k_{xp}, k_y - k_{yq}|^2 k_\rho dk_\rho d\phi.$$

Applying Parseval's theorem [21], we get

$$P_{pq} = \iint_A |A(x, y)|^2 dx\, dy. \tag{32}$$

Thus, the power integral (31) is determined by the amplitude of the aperture excitation $|A(x, y)|$, the directions of the grating lobes (θ_{pq}, ϕ_{pq}), and the embedded element radiation function $G(\theta, \phi)$. If the array antenna is designed to avoid grating lobes when the main beam direction θ_0 is steered over $[0, \theta_{\max}]$ in $\phi = \phi_0$ plane, we get

$$P = |G(\theta_0, \phi_0)|^2 \frac{(2\pi)^2}{k^2 \cos\theta_0 (d_x d_y)^2} P_{pq}. \tag{33}$$

REFERENCES

[1] R. J. Mailloux, *Phased Array Antenna Handbook*. Norwood, MA, USA: Artech House, 2017.

[2] M. A. Johnson, "Phased-array beam steering by multiplex sampling," *Proc. IEEE*, vol. 56, no. 11, pp. 1801–1811, Nov. 1968.

[3] H. King, J. Wong, and C. Zamites, "Shaped-beam antennas for satellites," *IEEE Trans. Antennas Propag.*, vol. 14, no. 5, pp. 641–643, Sep. 1966.

[4] D. M. Pozar and B. Kaufman, "Design considerations for low sidelobe microstrip arrays," *IEEE Trans. Antennas Propag.*, vol. 38, no. 8, pp. 1176–1185, Aug. 1990.

[5] O. T. Von Ramm and S. W. Smith, "Beam steering with linear arrays," *IEEE Trans. Biomed. Eng.*, no. 8, pp. 438–452, 1983.

[6] R. C. Hansen, "Array pattern control and synthesis," *Proc. IEEE*, vol. 80, no. 1, pp. 141–151, Jan. 1992.

[7] J. L. Allen and B. Diamond, "Mutual coupling in array antennas," Massachusetts Inst. Technol., Lincoln Lab., Lexington, MA, USA, Rep. 424, 1966.

[8] H.-S. Lui, Y. Yu, H. T. Hui, J. Yang, and H. Ling, "Mutual coupling in antenna arrays," *Int. J. Antennas Propagat.*, to be published.

[9] D. Buck, K. F. Warnick, R. Maaskant, D. B. Davidson, and D. F. Kelley, "Measuring array mutual impedances using embedded element patterns," *IEEE Trans. Antennas Propag.*, vol. 71, no. 1, pp. 606–611, Jan. 2023.

[10] D. Pozar and D. Schaubert, "Scan blindness in infinite phased arrays of printed dipoles," *IEEE Trans. Antennas Propag.*, vol. 32, no. 6, pp. 602–610, Jun. 1984.

[11] L. Zhang, J. A. Castaneda, and N. G. Alexopoulos, "Scan blindness free phased array design using PBG materials," *IEEE Trans. Antennas Propag.*, vol. 52, no. 8, pp. 2000–2007, Aug. 2004.

[12] C. Balanis, "Pattern distortion due to edge diffractions," *IEEE Trans. Antennas Propag.*, vol. 18, no. 4, pp. 561–563, Jul. 1970.

[13] G. Borgiotti, "Edge effects in finite arrays of uniform slits on a ground plane," *IEEE Trans. Antennas Propag.*, vol. 19, no. 5, pp. 593–599, Sep. 1971.

[14] P. Khanal, J. Yang, M. Ivashina, A. Höök, and R. Luo, "Edge truncation effects in a wide-scan phased array of connected Bowtie antenna elements," in *Proc. 14th Eur. Conf. Antennas Propagat. (EuCAP)*, 2020, pp. 1–5.

[15] P. Hannan, "The element-gain paradox for a phased-array antenna," *IEEE Trans. Antennas Propag.*, vol. 12, no. 4, pp. 423–433, Jul. 1964.

[16] J. J. Schuss, "Numerical design of patch radiator arrays," *Electromagnetics*, vol. 11, no. 1, pp. 47–68, 1991.

[17] H. Zhang, S. Yang, S.-W. Xiao, Y. Chen, S.-W. Qu, and J. Hu, "Ultrawideband phased antenna arrays based on tightly coupled open folded dipoles," *IEEE Antennas Wireless Propag. Lett.*, vol. 18, no. 2, pp. 378–382, Feb. 2019.

[18] R.-L. Xia, S.-W. Qu, S. Yang, and Y. Chen, "Wideband wide-scanning phased array with connected backed cavities and parasitic striplines," *IEEE Trans. Antennas Propag.*, vol. 66, no. 4, pp. 1767–1775, Apr. 2018.

[19] C.-M. Liu, S.-Q. Xiao, H.-L. Tu, and Z. Ding, "Wide-angle scanning low profile phased array antenna based on a novel magnetic dipole," *IEEE Trans. Antennas Propag.*, vol. 65, no. 3, pp. 1151–1162, Mar. 2017.

[20] X. Xia et al., "Millimeter-wave phased array antenna integrated with the industry design in 5G/B5G smartphones," *IEEE Trans. Antennas Propag.*, vol. 71, no. 2, pp. 1883–1888, Feb. 2023.

[21] P.-S. Kildal, *Foundations of Antenna Engineering: A Unified Approach for Line-of-Sight and Multipath*. Boston, MA, USA: Artech House, 2015.

[22] P. Khanal, J. Yang, M. Ivashina, A. Höök, and R. Luo, "A wide scanning array of connected Bowtie antennas suitable for integration in composite sandwich structures with monte-carlo tolerance analysis," *IEEE Access*, vol. 9, pp. 146691–146702, 2021.

[23] P. Khanal et al., "A wide-scanning array antenna of connected vertical Bowtie elements structurally integrated within an aircraft fuselage," *IEEE Trans. Antennas Propag.*, vol. 71, no. 5, pp. 4216–4227, May 2023.

[24] S. M. Moghaddam, J. Yang, and A. U. Zaman, "Fully-planar ultra-wideband tightly-coupled array (FPU-TCA) with integrated feed for wide-scanning millimeter-wave applications," *IEEE Trans. Antennas Propag.*, vol. 68, no. 9, pp. 6591–6601, Sep. 2020.

[25] C. A. Balanis, *Antenna Theory: Analysis and Design*. Hoboken, NJ, USA: Wiley, 2016.

[26] C. Wu, "Analysis of finite parallel-plate waveguide arrays," *IEEE Trans. Antennas Propag.*, vol. 18, no. 3, pp. 328–334, May 1970.

PRABHAT KHANAL (Graduate Student Member, IEEE) received the B.S. degree in electrical engineering from the Helsinki Metropolia University of Applied Sciences, Helsinki, Finland, in 2016, and the M.S. degree in electrical engineering from the Aalto University, Espoo, Finland, in 2018. He is currently pursuing the Ph.D. degree in electrical engineering with the Chalmers University of Technology, Gothenburg, Sweden. His research interests are wide-scanning phased array antennas and their applications.

JIAN YANG (Senior Member, IEEE) received the B.S. degree in electrical engineering from the Nanjing University of Science and Technology, Nanjing, China, in 1982, the M.S. degree in electrical engineering from the Nanjing Research Center of Electronic Engineering, Nanjing, China, in 1985, and the Swedish Licentiate and Ph.D. degrees from the Chalmers University of Technology, Gothenburg, Sweden, in 1998 and 2001, respectively. From 1985 to 1996, he was with the Nanjing Research Institute of Electronics Technology as a Senior Engineer. From 1999 to 2005, he was with the Department of Electromagnetics, Chalmers University of Technology as a Research Engineer. From 2005 to 2006, he was with COMHAT AB as a Senior Engineer. From 2006 to 2010, he was an Assistant Professor with the Department of Signals and Systems, Chalmers University of Technology. In 2010, 2016, and 2020, he has been an Associate Professor, a Professor, and a Full Professor, respectively, with the Department of Electrical Engineering, Chalmers University of Technology. He has published more than 89 journal articles and about 120 peer-reviewed conference papers. H-index: 34 and i10-index: 90. His research interests include ultra-wideband antennas and UWB feeds for reflector antennas, mmWave antennas, mmWave multilayer phased array antennas, mmWave sheet waveguide element antennas, gap waveguide antennas, UWB radar systems, UWB antennas in near-field sensing applications, hat-fed antennas, reflector antennas, radome design, and computational electromagnetics.